

Pressure-induced metal-insulator transition in oxygen-deficient LiNbO₃-type ferroelectrics

Chengliang Xia^{1,2}, Yue Chen¹ and Hanghui Chen^{2,3}

¹*Department of Mechanical Engineering,*

The University of Hong Kong,

Pokfulam Road, Hong Kong SAR, China

²*NYU-ECNU Institute of Physics,*

NYU Shanghai, Shanghai, 200062, China

³*Department of Physics,*

New York University,

New York 10003, USA

Abstract

Hydrostatic pressure and oxygen vacancies usually have deleterious effects on ferroelectric materials because both tend to reduce their polarization. In this work we use first-principles calculations to study an important class of ferroelectric materials – LiNbO₃-type ferroelectrics (LiNbO₃ as the prototype), and find that in oxygen-deficient LiNbO_{3- δ} , hydrostatic pressure induces an unexpected metal-insulator transition between 8 and 9 GPa. Our calculations also find that strong polar displacements persist in both metallic and insulating oxygen-deficient LiNbO_{3- δ} and the size of polar displacements is comparable to pristine LiNbO₃ under the same pressure. These properties are distinct from widely used perovskite ferroelectric oxide BaTiO₃, whose polarization is quickly suppressed by hydrostatic pressure and/or oxygen vacancies. The anomalous pressure-driven metal-insulator transition in oxygen-deficient LiNbO_{3- δ} arises from the change of an oxygen vacancy defect state. Hydrostatic pressure increases the polar displacements of oxygen-deficient LiNbO_{3- δ} , which reduces the band width of the defect state and eventually turns it into an in-gap state. In the insulating phase, the in-gap state is further pushed away from the conduction band edge under hydrostatic pressure, which increases the fundamental gap. Our work shows that for LiNbO₃-type strong ferroelectrics, oxygen vacancies and hydrostatic pressure combined can lead to new phenomena and potential functions, in contrast to the harmful effects occurring to perovskite ferroelectric oxides such as BaTiO₃.

I. INTRODUCTION

Ferroelectricity is one of the most important functional properties of transition metal oxides [1, 2]. Two classes of transition metal oxides: perovskite oxides (BaTiO₃ as the prototype) and small *A*-site LiNbO₃-type oxides (LiNbO₃ as the prototype) both exhibit robust ferroelectric polarization above room temperature [3–6], promising potential applications in ferroelectric-based electronic devices. The origin of ferroelectricity in BaTiO₃ arises from the hybridization between Ti-*d* and O-*p* states, which leads to a second-order Jahn-Teller distortion (SOJT) [7–9]. SOJT weakens the short-range repulsive forces that favor the non-polar structure and allows the long-range Coulombic forces to dominate, so that a polar structure is stabilized in BaTiO₃ [1, 10]. On the other hand, ferroelectricity in LiNbO₃ originates from a geometric mechanism rather than charge transfer or hybridization [11, 12]. The very small Li ion size (thus a tolerance factor $t < 1$) leads to a combined structural distortions of NbO₆ octahedral rotation and a Li polar displacement, which altogether optimize the Li-O bond length [13, 14]. For BaTiO₃, it is known that either hydrostatic (positive) pressure [15, 16] or (charge neutral) oxygen vacancies [17–21] can reduce its polarization, thereby limiting its applications under those unfavorable conditions [22–25]. Therefore it is interesting to explore how LiNbO₃ responds to oxygen vacancies and/or hydrostatic pressure. In our previous study, we carefully compare oxygen-deficient BaTiO_{3- δ} and LiNbO_{3- δ} *under ambient pressure* [26]. We find that in BaTiO_{3- δ} , the itinerant electrons doped by oxygen vacancies are uniformly distributed, but in LiNbO_{3- δ} , the distribution of itinerant electrons is highly inhomogeneous.

In this work, we extend our study to hydrostatic pressure effects on oxygen-deficient BaTiO_{3- δ} and LiNbO_{3- δ} . We find a more striking distinction between these two representative ferroelectric materials. For BaTiO₃, since either charge neutral oxygen vacancies or hydrostatic pressure tends to suppress its ferroelectric property, when these two factors are combined, expectedly it yields a more unfavorable condition for sustaining its polarization. Our first-principles calculations find that in oxygen-deficient BaTiO_{3- δ} , hydrostatic pressure can completely suppress its polarization and drive it into a paraelectric state. However, for LiNbO₃, in the presence of *both* charge neutral oxygen vacancies and external hydrostatic pressure, our calculations find an unexpected pressure-driven metal-insulator transition between 8 and 9 GPa, in a wide range of oxygen vacancy concentrations. The transition arises

from the change of an oxygen vacancy defect state in oxygen-deficient $\text{LiNbO}_{3-\delta}$, which is mainly composed of Nb- d orbitals. Applying a hydrostatic pressure increases the Nb-O polar displacements in $\text{LiNbO}_{3-\delta}$, due to a cooperative coupling between octahedral rotations and polarity [27]. This in turn reduces the band width of the defect state. When the applied pressure makes the band width of oxygen vacancy defect state sufficiently narrow in oxygen-deficient $\text{LiNbO}_{3-\delta}$, the defect state splits off the conduction bands and becomes an in-gap state, and thus the itinerant electrons get trapped around the oxygen vacancy and a metal-insulator transition occurs. Our calculations also find that in both metallic and insulating oxygen-deficient $\text{LiNbO}_{3-\delta}$, their polar displacements are comparable in magnitude to pristine LiNbO_3 under the same pressure. These robust polar properties imply that LiNbO_3 -based ferroelectric materials can have a wider range of applications, especially when they are under various conditions that are unfavorable to perovskite ferroelectrics such as BaTiO_3 .

II. COMPUTATIONAL DETAILS

We perform density functional theory (DFT) calculations [28, 29], as implemented in Vienna Ab-initio Simulation Package (VASP) [30, 31]. We use an energy cutoff of 600 eV. Charge self-consistent calculations are converged to 10^{-5} eV. Both cell and internal coordinates are fully relaxed until each force component is smaller than 10 meV/Å and stress tensor is smaller than 1 kbar. For the exchange-correlation functional, we use local spin density approximation (LSDA) [32]. However, we do not find magnetization in either pristine $\text{BaTiO}_3/\text{LiNbO}_3$ or oxygen-deficient $\text{BaTiO}_{3-\delta}/\text{LiNbO}_{3-\delta}$ (see Appendix A). Therefore we sum over both spins in the calculation of density of states. For pristine bulk calculations, we use a tetragonal cell (5-atom) with a Monkhorst-Pack \mathbf{k} -point sampling of $12 \times 12 \times 12$ to study BaTiO_3 and find that $a = 3.94$ Å and $c/a = 1.01$; we use a hexagonal cell (30-atom) with a Monkhorst-Pack \mathbf{k} -point sampling of $10 \times 10 \times 10$ to study $R3c$ LiNbO_3 and find that $a = 5.09$ Å and $c = 13.80$ Å. Both of them are in good agreement with the previous studies [33]. Bulk polarization is calculated using Berry phase method [34–36]. To study charge neutral oxygen vacancies, we use supercell calculations. For oxygen-deficient $\text{BaTiO}_{3-\delta}$, we start from the $P4mm$ structure of pristine BaTiO_3 and remove one charge neutral oxygen atom. There are two inequivalent Wyckoff positions for oxygen atoms in

the $P4mm$ structure [37]. We find similar results when oxygen vacancy is induced in either position. For oxygen-deficient $\text{LiNbO}_{3-\delta}$, we start from the $R3c$ structure of pristine LiNbO_3 and remove one charge neutral oxygen atom. There is only one Wyckoff position for oxygen atoms in the $R3c$ LiNbO_3 , i.e. all the oxygen atom positions are equivalent [38]. To simulate different oxygen vacancy concentrations, we use supercells of different sizes in which we remove one charge neutral oxygen vacancy. In the supercell calculations, we turn off all symmetries and fully relax the structure (both lattice constants and internal coordinates) to accommodate possible oxygen octahedral distortions and obtain the ground state property. We use a Monkhorst-Pack \mathbf{k} -point sampling of $8 \times 8 \times 8$ in supercell calculations. For the main results, we use a 59-atom supercell for $\text{BaTiO}_{3-\delta}$ and $\text{LiNbO}_{3-\delta}$ to simulate an oxygen vacancy concentration of $\delta = 8.3\%$. We also use a 79-atom, 119-atom and 179-atom supercell of $\text{LiNbO}_{3-\delta}$ to simulate a wide range of oxygen vacancy concentrations ($\delta = 6.3\%$, 4.2% and 2.8%) and test the robustness of our key results. We also use a higher energy cutoff (750 eV) and a denser \mathbf{k} -point sampling to test the key results and we do not find any qualitative difference.

III. RESULTS

For completeness and benchmarking, we first study hydrostatic pressure effects on pristine BaTiO_3 and LiNbO_3 . Then we compare oxygen-deficient $\text{BaTiO}_{3-\delta}$ and $\text{LiNbO}_{3-\delta}$ under hydrostatic pressure, and carefully study the pressure-driven metal-insulator transition in oxygen-deficient $\text{LiNbO}_{3-\delta}$.

A. Pressure effects on pristine BaTiO_3 and LiNbO_3

We summarize the hydrostatic pressure effects on pristine BaTiO_3 and LiNbO_3 in Fig. 1. In both BaTiO_3 and LiNbO_3 , the transition metal atoms (Ti and Nb) are in an oxygen octahedron and thus the crystal field splitting removes the d orbital degeneracy and separates the d orbitals into two energy groups [39]. The group with the lower (higher) energy is called t_{2g} (e_g) states. We focus on t_{2g} states for conciseness (we find similar results for e_g states). Panel **a** shows the band widths of Ti- t_{2g} and Nb- t_{2g} states as a function of applied hydrostatic pressure (the electronic band structures of pristine BaTiO_3 and LiNbO_3 under a

representative hydrostatic pressure are shown in Appendix B). Pressure naturally decreases the volumes of BaTiO_3 and LiNbO_3 (see panel **b**), which increases the hopping between Ti- d /Nb- d orbitals and O- p orbitals. As expected, the band width of both Ti- t_{2g} and Nb- t_{2g} states increases under hydrostatic pressure. However, as panel **a** shows, the band width of Nb- t_{2g} states increases much more slowly than that of Ti- t_{2g} states. To understand that, we compare the polar displacements (the definition of polar displacements in BaTiO_3 and LiNbO_3 can be found in Appendix C) and the polarization of BaTiO_3 and LiNbO_3 under hydrostatic pressure (panels **c** and **d**). Our calculations find that hydrostatic pressure reduces the polar displacements and polarization of BaTiO_3 and completely suppresses them above a critical value, due to the destabilization of short-range interaction at high pressure [15]. By contrast, our calculations find that hydrostatic pressure increases the polar displacements and polarization of LiNbO_3 , due to a cooperative coupling between octahedral rotations and polarity [27]. Similar results have been obtained in ferroelectric ZnSnO_3 [27] and polar metal LiOsO_3 [40]. This means that in LiNbO_3 , there are two competing forces: the overall volume reduction facilitates hopping, but the increased polar displacements make hopping more difficult; while in BaTiO_3 , both volume reduction and weakened polar displacements help increase hopping. Since band width is proportional to hopping, this explains why the band width of Nb- t_{2g} bands increases much more slowly than that of Ti- t_{2g} bands under hydrostatic pressure.

B. Pressure effects on oxygen-deficient $\text{BaTiO}_{3-\delta}$ and $\text{LiNbO}_{3-\delta}$

Next we study hydrostatic pressure effects on oxygen-deficient $\text{BaTiO}_{3-\delta}$ and oxygen-deficient $\text{LiNbO}_{3-\delta}$ and show that under pressure the electronic structure of these two materials behaves much more differently than pristine ones. Charge neutral oxygen vacancies are a common defect in complex oxides [41–45], which are electron donors and induce defect states that are close to conduction band edge [46–48]. If the band width of the defect states is large enough so that the Fermi level cuts through both defect bands and conduction bands, then the system is conducting and the doped electrons are itinerant.

Fig. 2 shows the density of states (DOS) of oxygen-deficient $\text{BaTiO}_{3-\delta}$ and $\text{LiNbO}_{3-\delta}$ (with $\delta = 8.3\%$) as a function of applied hydrostatic pressure. We find that under hydrostatic pressure, oxygen-deficient $\text{BaTiO}_{3-\delta}$ is conducting and its DOS almost does not change

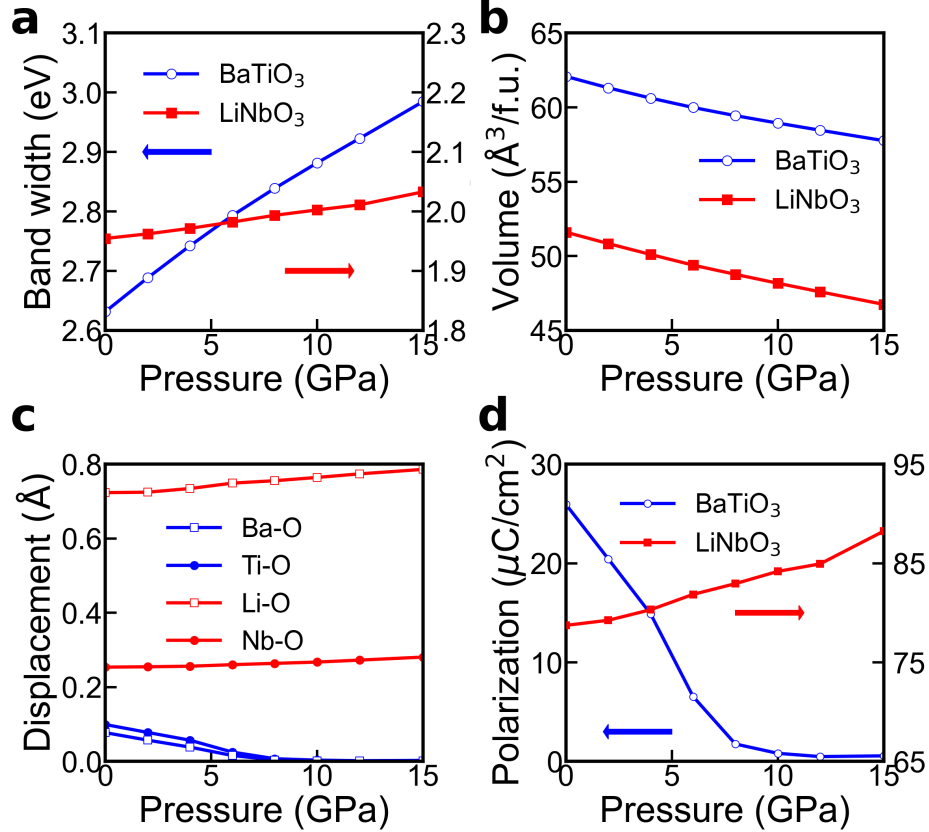


FIG. 1. Hydrostatic pressure effects on pristine BaTiO_3 and LiNbO_3 . As a function of hydrostatic pressure, **a**) the band width of $\text{Ti-}t_{2g}$ states of BaTiO_3 and $\text{Nb-}t_{2g}$ states of LiNbO_3 ; **b**) the volume of BaTiO_3 and LiNbO_3 per formula; **c**) Ba-O and Ti-O polar displacements of BaTiO_3 and Li-O and Nb-O polar displacements of LiNbO_3 ; **d**) the polarization of BaTiO_3 and LiNbO_3 .

under increasing pressure (panels **a**, **b**, **c**). By contrast, our calculations find that $\text{LiNbO}_{3-\delta}$ undergoes a metal-insulator transition. When the applied hydrostatic pressure is smaller than 8 GPa, $\text{LiNbO}_{3-\delta}$ is conducting; and above 8 GPa, a small gap is opened in the electronic structure of $\text{LiNbO}_{3-\delta}$ and the gap is further increased with pressure (see the insets of panels **e** and **f**). For pristine materials, this pressure-driven metal-insulator transition is rare, because pressure generically decreases volume and usually closes gap and makes materials more conducting.

To understand the origin of this pressure-driven metal-insulator transition, we study polar displacements (the definition of polar displacements in $\text{BaTiO}_{3-\delta}$ and $\text{LiNbO}_{3-\delta}$ is also found in Appendix C) and band structure of oxygen-deficient $\text{LiNbO}_{3-\delta}$ and compare them to those of oxygen-deficient $\text{BaTiO}_{3-\delta}$ (with $\delta = 8.3\%$). Fig. 3a shows the site-resolved Ti-O polar

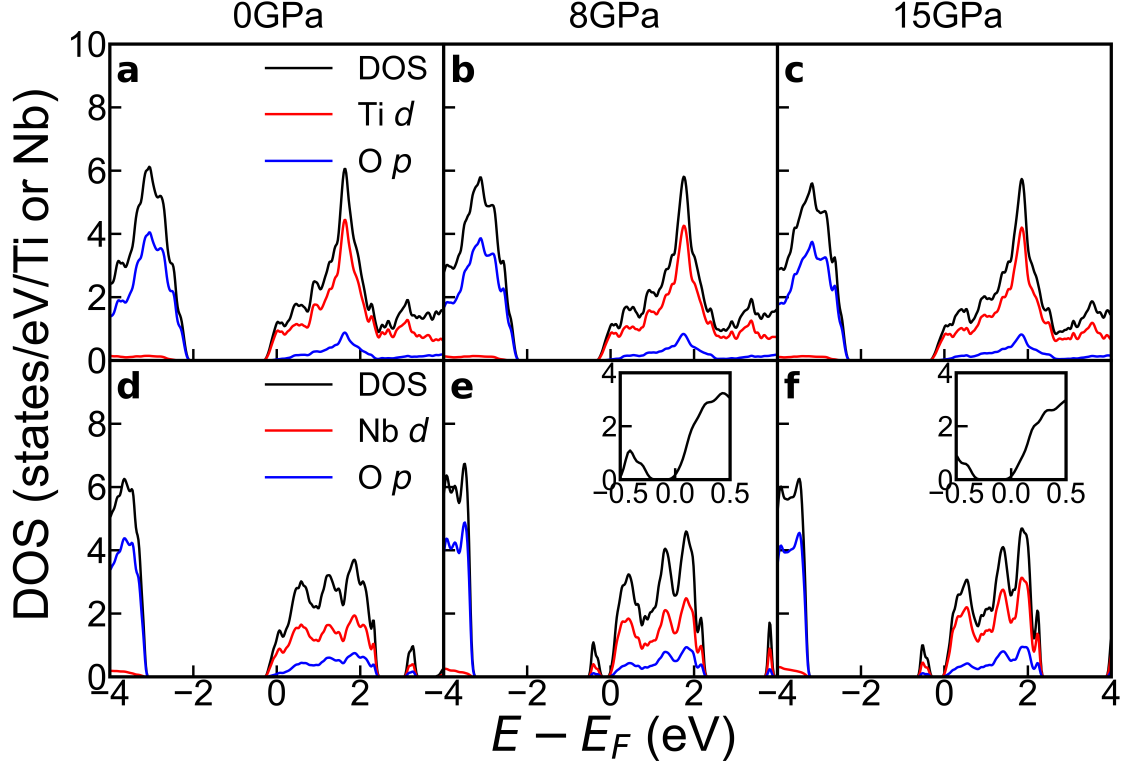


FIG. 2. Densities of states of oxygen-deficient $\text{BaTiO}_{3-\delta}$ (panels **a**, **b**, **c**) and oxygen-deficient $\text{LiNbO}_{3-\delta}$ (panels **d**, **e**, **f**) with $\delta = 8.3\%$ under a hydrostatic pressure of 0, 8 and 15 GPa, respectively. The black, red and blue are total, Ti- d or Nb- d and O- p projected densities of states, respectively. The insets in **e** and **f** show the densities of states near the Fermi level.

displacements in $\text{BaTiO}_{3-\delta}$ under hydrostatic pressure. Different from pristine BaTiO_3 , each oxygen vacancy donates two mobile electrons, which already suppress the average Ti-O polar displacements under ambient pressure. Applying a hydrostatic pressure does not affect the Ti-O polar displacements. Fig. 3**b** shows the electronic band structure of oxygen-deficient $\text{BaTiO}_{3-\delta}$. The lowest band that crosses the Fermi level is an oxygen vacancy defect state. Applying a hydrostatic pressure only slightly increases the band width of the defect state and has little effect on the overall electronic structure. Fig. 3**c** and **d** show the site-resolved Li-O and Nb-O polar displacements in oxygen-deficient $\text{LiNbO}_{3-\delta}$ under hydrostatic pressure. The red (blue) squares in Fig. 3**c** and **d** refer to the polar displacements in the conducting (insulating) $\text{LiNbO}_{3-\delta}$. In the inset of panel **d**, we compare the average Li-O and Nb-O polar displacements between oxygen-deficient $\text{LiNbO}_{3-\delta}$ and pristine LiNbO_3 under hydrostatic pressure. We find that similar to pristine LiNbO_3 (see Fig. 1), hydrostatic pressure increases

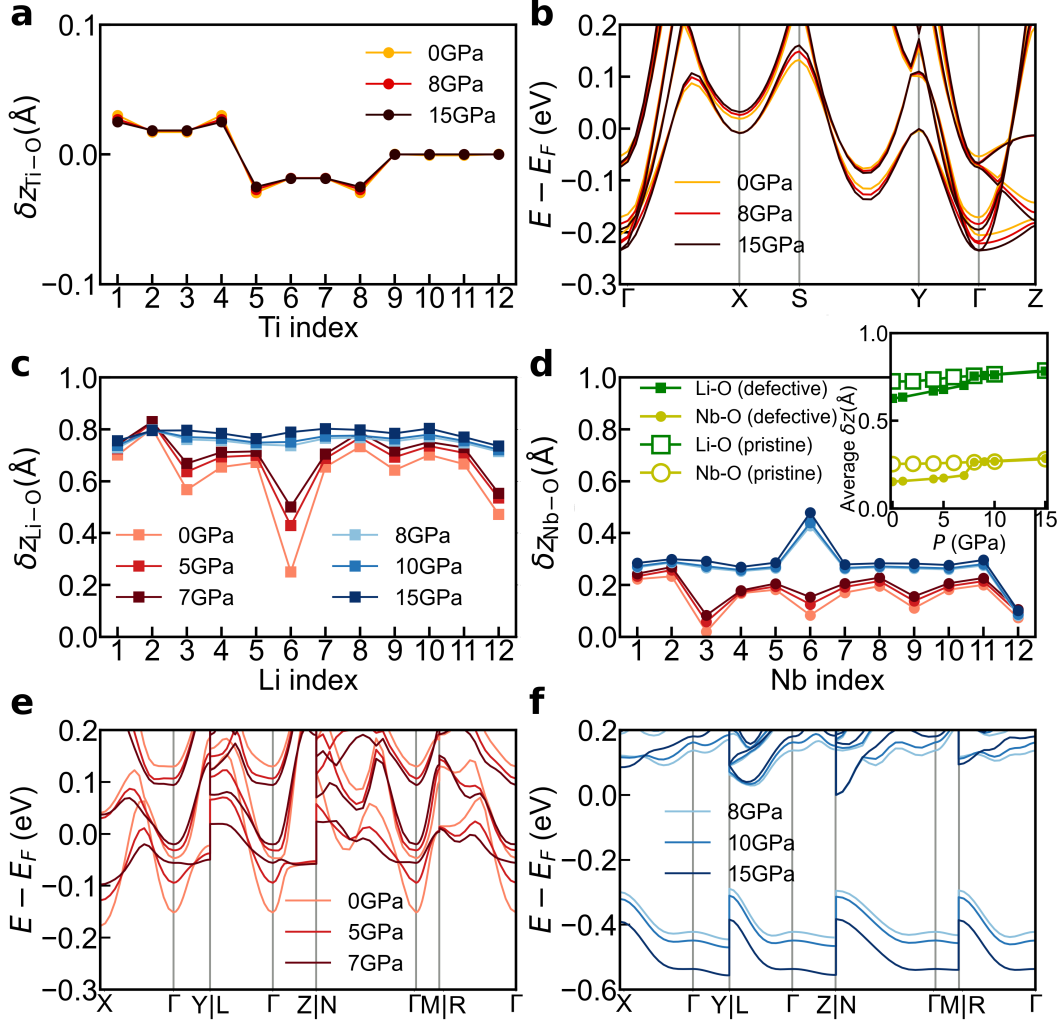


FIG. 3. Panels **a-b**: oxygen-deficient BaTiO_{3- δ} (with $\delta = 8.3\%$) under a hydrostatic pressure of 0, 8 and 15 GPa. **a**: polar displacements of each Ti atom. **b**: electronic band structure close to the Fermi level. The high-symmetry \mathbf{k} -path is $\Gamma(0,0,0)$ -X(0.5,0,0)-S(0.5,0.5,0)-Y(0,0.5,0)- $\Gamma(0,0,0)$ -Z(0,0,0.5). Panels **c-f**: oxygen-deficient LiNbO_{3- δ} (with $\delta = 8.3\%$) under several hydrostatic pressures in the range of 0-15 GPa. **c**: polar displacements of each Li atom. **d**: polar displacements of each Nb atom. Red and blue squares represent conducting and insulating phases of oxygen-deficient LiNbO_{3- δ} , respectively. The inset in **d** compares the average polar displacements of Li and Nb in oxygen-deficient LiNbO_{3- δ} (with $\delta = 8.3\%$) and pristine LiNbO₃. **e**: electronic band structure close to the Fermi level under a hydrostatic pressure of 0, 5 and 7 GPa, where LiNbO_{3- δ} is conducting. **f**: electronic band structure close to the Fermi level under a hydrostatic pressure of 8, 10 and 15 GPa, where LiNbO_{3- δ} is insulating. The high-symmetry \mathbf{k} -point path is X(0,-0.5,0)- $\Gamma(0,0,0)$ -Y(0.5,0,0)|L(0.5,-0.5,0)- $\Gamma(0,0,0)$ -Z(-0.5,0,0.5)|N(-0.5,-0.5,0.5)- $\Gamma(0,0,0)$ -M(0,0,0.5)|R(0,-0.5,0.5)- $\Gamma(0,0,0)$.

the polar displacements of oxygen-deficient $\text{LiNbO}_{3-\delta}$. In particular, the Nb atom and the Li atom that are closest to the oxygen vacancy have the most substantial increase in the polar displacement. However, different from pristine LiNbO_3 , there is a sudden “jump” in the polar displacements between 7 and 8 GPa, which is evident in the inset of panel **d**. For a given hydrostatic pressure, the average polar displacements of conducting oxygen-deficient $\text{LiNbO}_{3-\delta}$ are slightly smaller than those of pristine LiNbO_3 . This is because mobile electrons in conducting $\text{LiNbO}_{3-\delta}$ can screen internal electric fields and suppress the polar displacements [26]. However, in insulating $\text{LiNbO}_{3-\delta}$, the average polar displacements are almost the same as those of pristine LiNbO_3 because screening from mobile electrons is absent.

Accompanying this sudden “jump” in the polar displacements is a metal-insulator transition. Fig. 3e and f show the electronic band structures of conducting and insulating oxygen-deficient $\text{LiNbO}_{3-\delta}$, respectively. In conducting $\text{LiNbO}_{3-\delta}$, the band width of the defect state is reduced by hydrostatic pressure, which is in contrast to pristine LiNbO_3 and BaTiO_3 in which hydrostatic pressure always increases their band width. This anomalous pressure effect is because the defect state is closely related to Nb #6, which is the nearest neighbor of the oxygen vacancy. The substantially increased polar displacement of Nb #6 makes the electron hopping much more difficult, which overweighs the volume reduction from hydrostatic pressure. In insulating $\text{LiNbO}_{3-\delta}$, the defect state becomes an in-gap state. Similar to defects in semiconductors, hydrostatic pressure increases the repulsion between conduction band edge and in-gap states, which further increases the fundamental band gap of oxygen-deficient $\text{LiNbO}_{3-\delta}$ (i.e. the gap between the conduction band edge and the defect state) [49–53].

Next we study how hydrostatic pressure changes the spatial distribution of doped electrons in oxygen-deficient $\text{BaTiO}_{3-\delta}$ and oxygen-deficient $\text{LiNbO}_{3-\delta}$. Each oxygen vacancy donates two electrons and they occupy the defect state and conduction bands, which are mainly composed of Ti-*d* or Nb-*d* states. Fig. 4 shows the spatial distribution of doped electrons and the number of doped electrons on each Ti and Nb atoms in oxygen-deficient $\text{BaTiO}_{3-\delta}$ and $\text{LiNbO}_{3-\delta}$ (with $\delta = 8.3\%$). Oxygen-deficient $\text{BaTiO}_{3-\delta}$ is always conducting and the doped electrons are almost homogeneously distributed, as is shown explicitly in Fig. 4a and b. Hydrostatic pressure makes the electron distribution even more homogeneous in $\text{BaTiO}_{3-\delta}$ (see Fig. 4c). However, in oxygen-deficient $\text{LiNbO}_{3-\delta}$, the distribution

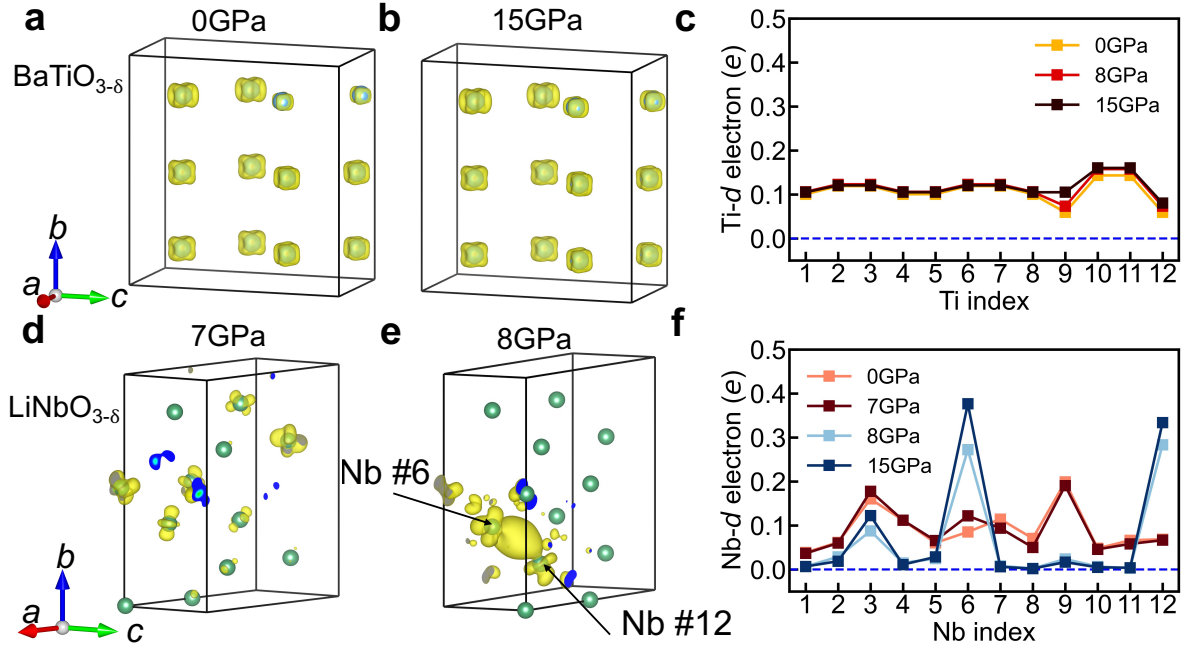


FIG. 4. Panels **a** and **b** show the iso-value surfaces of doped electron distribution in oxygen-deficient BaTiO_{3-δ} with $\delta = 8.3\%$ under 0 and 15 GPa, respectively. Panel **c** shows the doped electrons on each Ti atom in oxygen-deficient BaTiO_{3-δ} ($\delta = 8.3\%$) under a hydrostatic pressure of 0, 8 and 15 GPa. Panels **d** and **e** are the iso-value surfaces of doped electron distribution in oxygen-deficient LiNbO_{3-δ} with $\delta = 8.3\%$ under 7 and 8 GPa, respectively. Panel **f** shows the doped electrons on each Nb atom in oxygen-deficient LiNbO_{3-δ} ($\delta = 8.3\%$) under a hydrostatic pressure of 0, 7, 8 and 15 GPa. For both materials, the iso-surface corresponds to a charge density of $0.027e/\text{\AA}^3$. The number of doped electrons on each Ti or Nb atom is obtained by integrating their *d* states from the valence band edge to the Fermi level.

of doped electrons is highly inhomogeneous [26]. As we showed previously in Fig. 3, hydrostatic pressure increases the polar displacements of LiNbO_{3-δ} and narrows the band width of the defect state, which means the reduction of electron hopping. Correspondingly, the doped electrons tend to be localized in real space. From ambient pressure to 7 GPa, the doped electrons are distributed on all Nb sites (see Fig. 4d). However, under a hydrostatic pressure of 8 GPa that is just above the critical pressure, most doped electrons are concentrated in the void space between Nb #6 and Nb #12, which are the two nearest neighbors of the oxygen vacancy (see Fig. 4e). Such a localization effect can be more clearly seen from the two peaks in the Nb site-resolved electron distribution, shown in Fig. 4f. In oxygen-

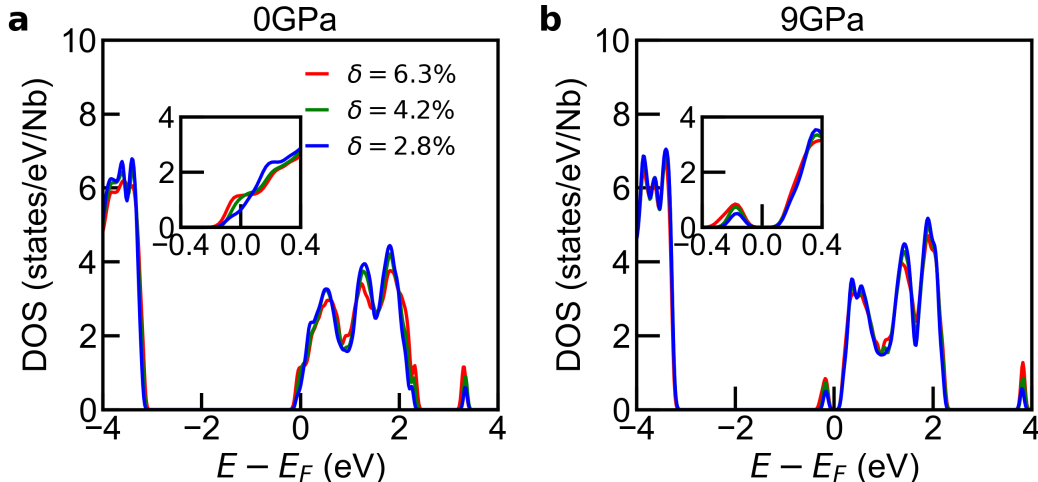


FIG. 5. Densities of states of oxygen-deficient $\text{LiNbO}_{3-\delta}$ with different vacancy concentrations under 0 (panel **a**) and 9 GPa (panel **b**). The red, green and blue curves are for $\text{LiNbO}_{3-\delta}$ with $\delta = 6.3\%$, $\delta = 4.2\%$ and $\delta = 2.8\%$, respectively. The insets show the densities of states near the Fermi level.

deficient $\text{LiNbO}_{3-\delta}$, applying hydrostatic pressure localizes itinerant electrons and leads to a metal-insulator transition, in stark contrast to oxygen-deficient $\text{BaTiO}_{3-\delta}$. We note that the localized carriers in the insulating $\text{LiNbO}_{3-\delta}$ (Fig. 4e) correspond to *two* electrons that are donated by an oxygen vacancy. These two electrons completely fill the defect band (see Fig. 3f) and thus spin up and spin down channels have equal occupancy. Therefore, no local magnetic moment emerges from this charge localization. Our case is different from a recent work on doped BaTiO_3 under epitaxial strain [54] in which *one* electron half-fills a band and occupies a single spin channel. Correlation effects localize the lone electron and a magnetic polaron state is formed [55].

So far, we have only studied one concentration of oxygen vacancy $\delta = 8.3\%$. In Fig. 5 we study different oxygen vacancy concentrations in oxygen-deficient $\text{LiNbO}_{3-\delta}$. We find that the pressure-driven metal-insulator transition occurs in a wide range of vacancy concentrations. In addition to $\delta = 8.3\%$ (59-atom cell), we also calculate $\delta = 6.3\%$ (79-atom cell), $\delta = 4.2\%$ (119-atom) and 2.8% (179-atom cell). In all three cases, under ambient pressure, $\text{LiNbO}_{3-\delta}$ is conducting (Fig. 5a) while under a hydrostatic pressure of 9 GPa, $\text{LiNbO}_{3-\delta}$ becomes insulating with the defect state turning into an in-gap state and lying below the conduction bands (Fig. 5b). The critical pressure weakly depends on vacancy concentration,

which ranges between 8 and 9 GPa for oxygen-deficient $\text{LiNbO}_{3-\delta}$.

Finally, we make two comments. One is that the pressure-driven metal-insulator transition in our study is fundamentally different from the pressure-driven insulator-to-metal transition in correlated materials [56–59]. In the former, high pressure stabilizes an *insulating* state in oxygen-deficient $\text{LiNbO}_{3-\delta}$; while in the latter, increasing pressure closes the Mott gap and leads to a *metallic* state. The pressure-driven insulator-to-metal transition in correlated materials is usually strongly first-order, accompanied by abrupt reduction in volume and/or collapse of local magnetic moment [60–62]. By contrast, the pressure-driven metal-insulator transition in our study is associated with a defect band, which is fully occupied when the fundamental gap is opened. As we mentioned above, since the defect band is fully occupied (in both spin up and spin down channels), no local magnetic moment is found in our calculations and correlation effects play a minor role. The second comment is the connection between our results and available experimental data. Oxygen vacancies have been widely found in important ferroelectric oxides, such as BaTiO_3 [63], PbTiO_3 [64], $(\text{Pb}_{1-x}\text{Ba}_x)(\text{Zr}_{0.95}\text{Ti}_{0.05})\text{O}_3$ [65, 66], KNbO_3 [67], LiNbO_3 [68], HfO_2 [69, 70], and amorphous Al_2O_3 [71]. The presence of oxygen vacancies can substantially change the structural, dielectric, and transport properties of ferroelectrics [22, 25], such as the reduction of polarization [72, 73] and the emergence of conduction [65, 67]. Sometimes combining oxygen vacancies and polar structure in ferroelectrics can also lead to new functions [71, 74, 75]. Most pertinent to the current study are oxygen-deficient $\text{BaTiO}_{3-\delta}$ and $\text{LiNbO}_{3-\delta}$. Oxygen vacancies in BaTiO_3 have been observed and studied in a few experiments [19–21]. The theoretical results in the current study are qualitatively consistent with the experiments in that 1) conduction appears in $\text{BaTiO}_{3-\delta}$ due to oxygen vacancies [19, 20]; 2) Ti-O polar displacements are reduced by itinerant electrons and are completely suppressed above a critical electron concentration of $1.9 \times 10^{21} \text{ cm}^{-3}$ [21]. For LiNbO_3 , various types of defects such as Li-vacancies, O-vacancies, Li-Nb antisite defects, etc. are found in experiments [76–79]. In particular, oxygen-deficient $\text{LiNbO}_{3-\delta}$ in nanocrystallites and single crystals have been reported in several experiments [80–83], but high-pressure study has not been performed. We hope that our theoretical study may stimulate further experiments on oxygen-deficient $\text{LiNbO}_{3-\delta}$ under hydrostatic pressure.

IV. CONCLUSION

In summary, we compare the pressure effects on two important and representative ferroelectric oxides BaTiO_3 and LiNbO_3 in the pristine form and in a defective form with oxygen vacancies. In pristine BaTiO_3 , hydrostatic pressure reduces the polar displacements and increases the band width of Ti- d states. In oxygen-deficient $\text{BaTiO}_{3-\delta}$, pressure makes the doped electrons more homogeneously distributed. Both phenomena are within expectation. By contrast, in both pristine LiNbO_3 and oxygen-deficient $\text{LiNbO}_{3-\delta}$, pressure increases their polar displacements. More strikingly, in oxygen-deficient $\text{LiNbO}_{3-\delta}$, we find an unexpected pressure-driven metal-insulator transition. The anomalous transition arises from the fact that the substantially increased polar displacements in oxygen-deficient $\text{LiNbO}_{3-\delta}$ under hydrostatic pressure reduce the overlap between Nb- d and O- p orbitals and thus decrease the band width of the defect state. When the band width of the defect state is sufficiently narrow, it turns into an in-gap state and the system becomes insulating with itinerant electrons trapped around the oxygen vacancy. This pressure-driven metal-insulator transition occurs to oxygen-deficient $\text{LiNbO}_{3-\delta}$ in a wide range of oxygen vacancy concentrations.

Our work shows that LiNbO_3 -type ferroelectric materials have more robust polar properties against oxygen vacancies and hydrostatic pressure than BaTiO_3 . Furthermore, the intriguing pressure-driven metal-insulator transition in oxygen-deficient $\text{LiNbO}_{3-\delta}$ is not found in widely used ferroelectric materials BaTiO_3 or $\text{BaTiO}_{3-\delta}$. This implies that LiNbO_3 -based ferroelectric devices may have a wider range of applications, in particular when they are under conditions that are unfavorable to perovskite ferroelectrics such as BaTiO_3 .

ACKNOWLEDGMENTS

Hanghui Chen is supported by the National Natural Science Foundation of China under project number 11774236 and NYU University Research Challenge Fund. Yue Chen and Chengliang Xia are supported by the Research Grants Council of Hong Kong under Project Number 17201019. The authors are grateful for the research computing facilities offered by ITS, HKU and high-performance computing resources from NYU Shanghai.

Appendix A: LSDA calculations for possible magnetization

In this section, we show the LSDA calculations of pristine BaTiO_3 and LiNbO_3 , as well as oxygen-deficient $\text{BaTiO}_{3-\delta}$ and $\text{LiNbO}_{3-\delta}$. We find that while we intentionally break the spin symmetry, the resulting density of states do not exhibit any magnetization in our calculations.

Fig. 6 shows the density of states of pristine BaTiO_3 and LiNbO_3 under a hydrostatic pressure of 0, 8 and 15 GPa. Fig. 7 shows the density of states of oxygen-deficient $\text{BaTiO}_{3-\delta}$ and $\text{LiNbO}_{3-\delta}$ under a hydrostatic pressure of 0, 8 and 15 GPa.

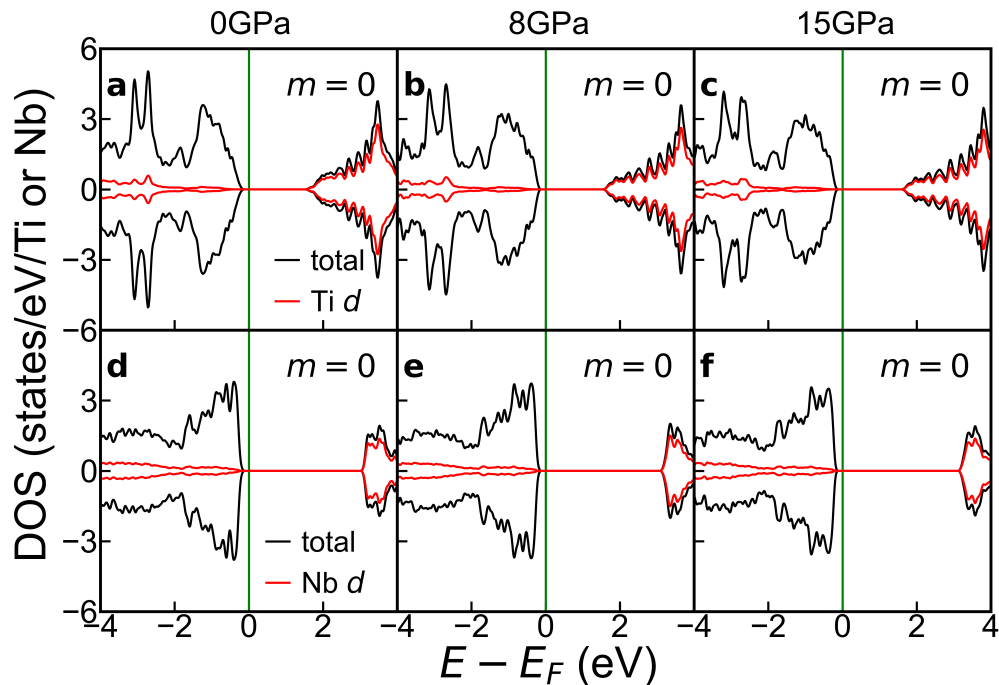


FIG. 6. Densities of states of pristine BaTiO_3 (panels **a**, **b**, **c**) and pristine LiNbO_3 (panels **d**, **e**, **f**) under a hydrostatic pressure of 0, 8 and 15 GPa. The black and red lines are total and Ti- d /Nb- d projected densities of states, respectively. m shown in each sub-plot is the average magnetization per Ti or per Nb. The green solid line is the Fermi level.

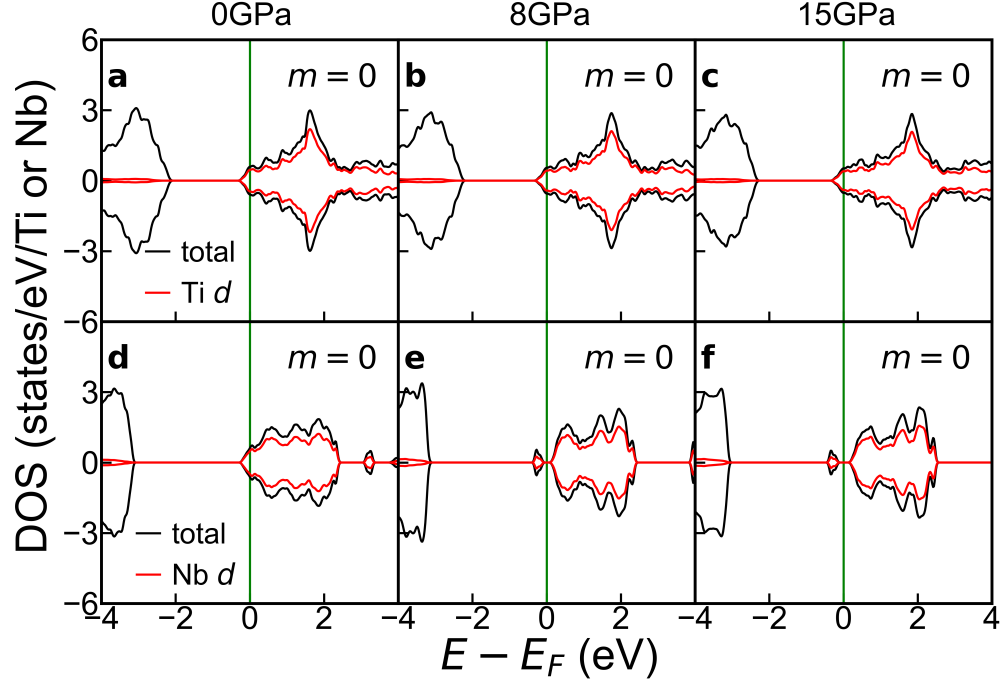


FIG. 7. Densities of states of oxygen-deficient $\text{BaTiO}_{3-\delta}$ (panels **a**, **b**, **c**) and oxygen-deficient $\text{LiNbO}_{3-\delta}$ (panels **d**, **e**, **f**) with $\delta = 8.3\%$ under a hydrostatic pressure of 0, 8 and 15 GPa. The black and red lines are total and Ti- d /Nb- d projected densities of states, respectively. m shown in each sub-plot is the average magnetization per Ti or per Nb. The green solid line is the Fermi level.

Appendix B: Electronic band structure of pristine BaTiO₃ and LiNbO₃ under a hydrostatic pressure

Fig. 8 shows densities of states and electronic band structure of pristine BaTiO₃ (panels **a** and **c**) and pristine LiNbO₃ (panels **b** and **d**) under a representative hydrostatic pressure of 8 GPa. Both pristine BaTiO₃ and LiNbO₃ are wide gap insulators under ambient pressure and they remain insulating under a hydrostatic pressure of 8 GPa. In the calculations, we find that the overall electronic structures of BaTiO₃ and LiNbO₃ do not change substantially with pressure but the band width of Ti-*d* and Nb-*d* states increase under pressure. Since we are interested in the band width of Ti-*d* and Nb-*d* states, we only show the electronic band structure above the conduction band minimum (CBM). Due to the crystal field splitting in BaTiO₃ and LiNbO₃, both Ti-*d* and Nb-*d* orbitals are split into *t*_{2g} and *e*_g states. The Ti-*t*_{2g} and Nb-*t*_{2g} states are highlighted in red in panels **c** and **d** of Fig. 8. Our calculations find that the band width of both *t*_{2g} and *e*_g states increase under pressure. For conciseness, we only show the pressure dependence of Ti-*t*_{2g} and Nb-*t*_{2g} band width in Fig. 1 in the main text.

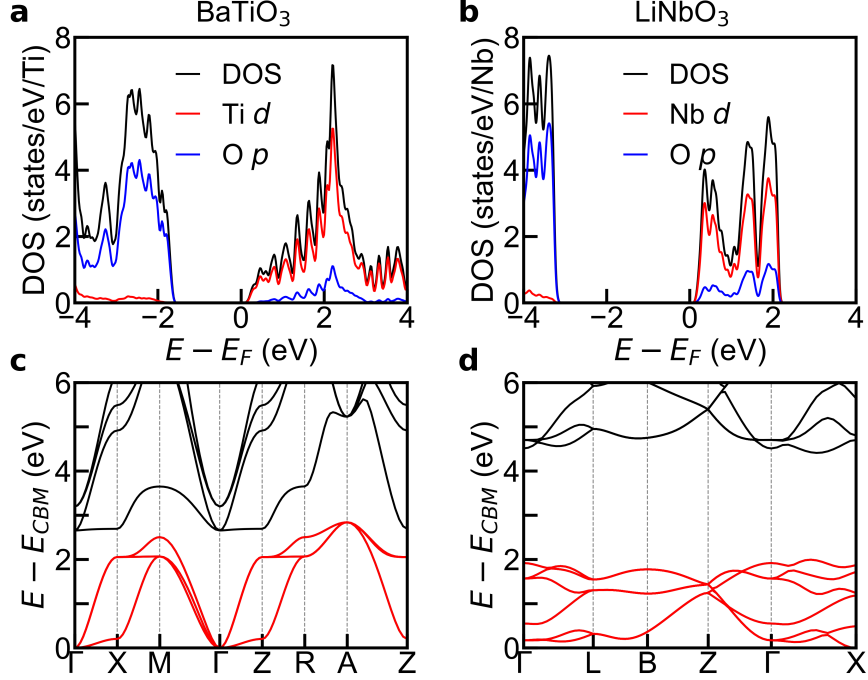


FIG. 8. Densities of states and electronic band structure of pristine BaTiO₃ (panels **a** and **c**) and pristine LiNbO₃ (panels **b** and **d**) under a hydrostatic pressure of 8 GPa. The black, red, and blue lines in **a** and **b** are total, Ti-*d* or Nb-*d*, and O-*p* projected densities of states, respectively. Only those energy bands that are above the conduction band minimum (CBM) are shown in **c** and **d**. Ti-*t*_{2g} and Nb-*t*_{2g} states are highlighted in red. The high-symmetry **k**-path of BaTiO₃ is $\Gamma(0,0,0)$ -X(0.5,0,0)-M(0.5,0.5,0)- $\Gamma(0,0,0)$ -Z(0,0,0.5)-R(0,0.5,0.5)-A(0.5,0.5,0.5)-Z(0,0,0.5). The high-symmetry **k**-path of LiNbO₃ is $\Gamma(0,0,0)$ -L(0.5,0,0)-B(0.5,0.236,-0.236)-Z(0.5,0.5,0.5)- $\Gamma(0,0,0)$ -X(0.368,0,-0.368).

Appendix C: Definition of polar displacements

The advantage of using polar displacements to characterize ferroelectric-like distortions is that they are well defined in both insulating and conducting systems, while polarization is ill-defined in metals [22, 84, 85].

Pristine BaTiO_3 and LiNbO_3 are both insulators. However, oxygen vacancies donate itinerant electrons and make oxygen-deficient $\text{BaTiO}_{3-\delta}$ and $\text{LiNbO}_{3-\delta}$ conducting under ambient pressure. We follow the previous definition of polar displacements when we study BaTiO_3 and LiNbO_3 under ambient pressure [26] and now extend the definition to the case in which both materials are under hydrostatic pressure. For self-containedness, we outline the definition of polar displacement δz briefly below.

Fig. 9a and b show the crystal structure of pristine BaTiO_3 and oxygen-deficient $\text{BaTiO}_{3-\delta}$ with $\delta = 8.3\%$. In the ab plane, each Ti atom is surrounded by four O atoms in TiO_2 layer and Ti atoms move along the c axis, therefore Ti-O displacement $\delta z_{\text{Ti-O}}$ is defined as:

$$\delta z_{\text{Ti-O}} = z_{\text{Ti}} - \frac{1}{4} \sum_{i=1}^4 z_{\text{O}_i} \quad (\text{C1})$$

where z_{Ti} is the c position of Ti and z_{O_i} is the c position of the four nearest O atoms. $\delta z_{\text{Ba-O}}$ is defined in a similar way as $\delta z_{\text{Ti-O}}$. We note that in oxygen-deficient $\text{BaTiO}_{3-\delta}$, the two Ti atoms that are closest to the oxygen vacancy only have three nearest O atoms in TiO_2 layer in ab plane, therefore the Ti-O displacement $\delta z_{\text{Ti-O}}$ for these two Ti atoms is defined as:

$$\delta z_{\text{Ti-O}} = z_{\text{Ti}} - \frac{1}{3} \sum_{i=1}^3 z_{\text{O}_i} \quad (\text{C2})$$

where z_{O_i} is the c position of the three nearest O atoms around the Ti atom in ab plane.

Fig. 9c and d show the crystal structure of pristine LiNbO_3 and oxygen-deficient $\text{LiNbO}_{3-\delta}$ with $\delta = 8.3\%$. $\delta z_{\text{Li-O}}$ and $\delta z_{\text{Nb-O}}$ are defined in slightly different ways. Each Li atom is surrounded by three O atoms and Li atoms move along the c axis. Li-O displacement $\delta z_{\text{Li-O}}$ is defined as:

$$\delta z_{\text{Li-O}} = z_{\text{Li}} - \frac{1}{3} \sum_{i=1}^3 z_{\text{O}_i} \quad (\text{C3})$$

where z_{Li} is the c position of Li and z_{O_i} is the c position of the three nearest O atoms. Each Nb atom is surrounded by six O atoms and Nb atoms move along the c axis. Nb-O

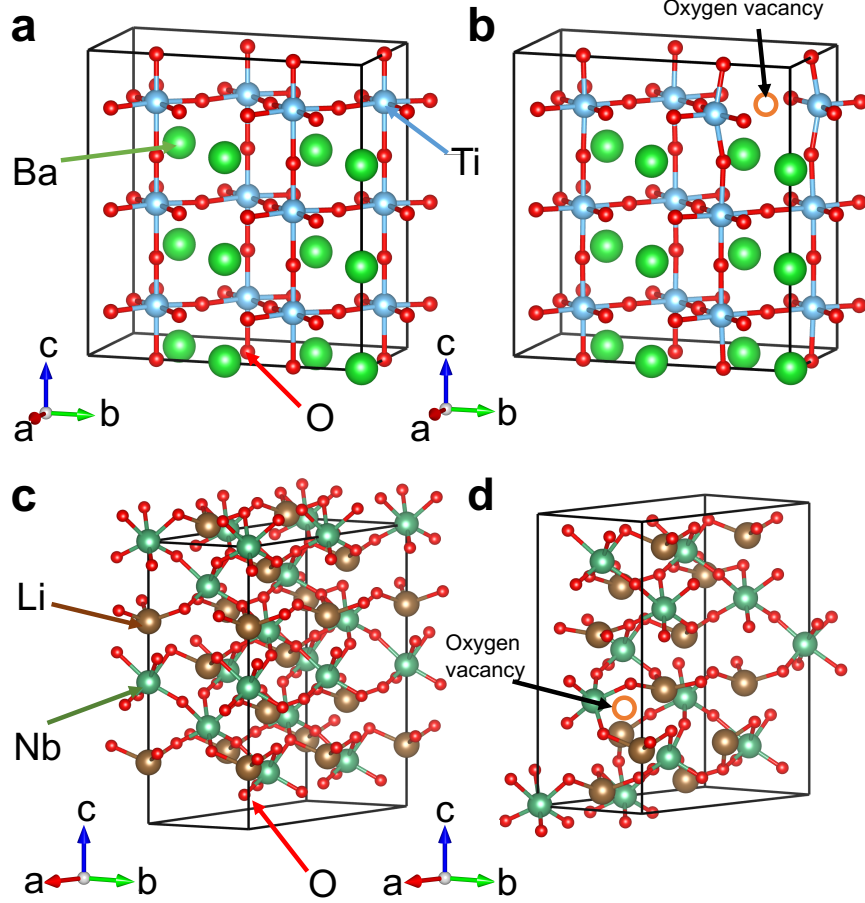


FIG. 9. Crystal structures of pristine BaTiO_3 (panel **a**), oxygen-deficient $\text{BaTiO}_{3-\delta}$ with $\delta = 8.3\%$ (panel **b**), pristine LiNbO_3 (panel **c**) and oxygen-deficient $\text{LiNbO}_{3-\delta}$ with $\delta = 8.3\%$ (panel **d**). Green, blue and red balls in panels **a** and **b** are Ba, Ti and O atoms, respectively. Brown, green and red balls in panels **c** and **d** are Li, Nb and O atoms, respectively. The oxygen vacancy in oxygen-deficient $\text{BaTiO}_{3-\delta}$ and $\text{LiNbO}_{3-\delta}$ is highlighted by the orange open circle.

displacement $\delta z_{\text{Nb-O}}$ is defined as:

$$\delta z_{\text{Nb-O}} = z_{\text{Nb}} - \frac{1}{6} \sum_{i=1}^6 z_{\text{O}_i} \quad (\text{C4})$$

where z_{Nb} is the c position of Nb and z_{O_i} is the c position of the six nearest O atoms. We note that in oxygen-deficient $\text{LiNbO}_{3-\delta}$, the Li atom that is closest to the oxygen vacancy only has two nearest O atoms, and the two Nb atoms that are closest to the oxygen vacancy only have five nearest O atoms. Therefore, the Li-O displacement for this Li atom and the

Nb-O displacement for these two Nb atoms are defined as:

$$\delta z_{\text{Li-O}} = z_{\text{Li}} - \frac{1}{2} \sum_{i=1}^2 z_{\text{O}_i} \quad (\text{C5})$$

where z_{O_i} is c position of the two nearest O atoms for the Li atom and

$$\delta z_{\text{Nb-O}} = z_{\text{Nb}} - \frac{1}{5} \sum_{i=1}^5 z_{\text{O}_i} \quad (\text{C6})$$

where z_{O_i} is c position of the five nearest O atoms around the Nb atom.

-
- [1] R. E. Cohen, *Nature* **358**, 136 (1992).
- [2] T. Goto, T. Kimura, G. Lawes, A. P. Ramirez, and Y. Tokura, *Phys. Rev. Lett.* **92**, 257201 (2004).
- [3] I. Inbar and R. E. Cohen, *Phys. Rev. B* **53**, 1193 (1996).
- [4] M. B. Smith, K. Page, T. Siegrist, P. L. Redmond, E. C. Walter, R. Seshadri, L. E. Brus, and M. L. Steigerwald, *Journal of the American Chemical Society* **130**, 6955 (2008).
- [5] Y. Inaguma, M. Yoshida, and T. Katsumata, *Journal of the American Chemical Society* **130**, 6704 (2008).
- [6] Y. Shi, Y. Guo, X. Wang, A. J. Princep, D. Khalyavin, P. Manuel, Y. Michiue, A. Sato, K. Tsuda, S. Yu, et al., *Nature Materials* **12**, 1024 (2013).
- [7] I. Bersuker, *Physics Letters* **20**, 589 (1966).
- [8] I. B. Bersuker and B. Vekhter, *Ferroelectrics* **19**, 137 (1978).
- [9] J. K. Burdett, *Inorganic Chemistry* **20**, 1959 (1981).
- [10] I. B. Bersuker, *Journal of Physics: Conference Series* **428**, 012028 (2013).
- [11] C. Ederer and N. A. Spaldin, *Phys. Rev. B* **74**, 024102 (2006).
- [12] N. A. Benedek and C. J. Fennie, *The Journal of Physical Chemistry C* **117**, 13339 (2013).
- [13] A. Navrotsky, *Chemistry of Materials* **10**, 2787 (1998).
- [14] N. A. Benedek and T. Birol, *J. Mater. Chem. C* **4**, 4000 (2016).
- [15] E. Bousquet and P. Ghosez, *Phys. Rev. B* **74**, 180101 (2006).
- [16] J. J. Wang, P. P. Wu, X. Q. Ma, and L. Q. Chen, *Journal of Applied Physics* **108**, 114105 (2010).
- [17] I.-K. Jeong, S. Lee, S.-Y. Jeong, C. J. Won, N. Hur, and A. Llobet, *Phys. Rev. B* **84**, 064125 (2011).
- [18] M. Choi, F. Oba, and I. Tanaka, *Applied Physics Letters* **98**, 172901 (2011).
- [19] T. Kolodiaznyi, *Phys. Rev. B* **78**, 045107 (2008).
- [20] J. Hwang, T. Kolodiaznyi, J. Yang, and M. Couillard, *Phys. Rev. B* **82**, 214109 (2010).
- [21] T. Kolodiaznyi, M. Tachibana, H. Kawaji, J. Hwang, and E. Takayama-Muromachi, *Phys. Rev. Lett.* **104**, 147602 (2010).
- [22] Y. Wang, X. Liu, J. D. Burton, S. S. Jaswal, and E. Y. Tsymlal, *Phys. Rev. Lett.* **109**, 247601

- (2012).
- [23] D. Hickox-Young, D. Puggioni, and J. M. Rondinelli, *Phys. Rev. B* **102**, 014108 (2020).
 - [24] V. F. Michel, T. Esswein, and N. A. Spaldin, *J. Mater. Chem. C* **9**, 8640 (2021).
 - [25] J. Ma, R. Yang, and H. Chen, *Nat. Commun.* **12**, 1 (2021).
 - [26] C. Xia, Y. Chen, and H. Chen, *Phys. Rev. Materials* **3**, 054405 (2019).
 - [27] T. Gu, T. Scarbrough, Y. Yang, J. Íñiguez, L. Bellaiche, and H. J. Xiang, *Phys. Rev. Lett.* **120**, 197602 (2018).
 - [28] P. Hohenberg and W. Kohn, *Phys. Rev.* **136**, B864 (1964).
 - [29] W. Kohn and L. J. Sham, *Phys. Rev.* **140**, A1133 (1965).
 - [30] M. C. Payne, M. P. Teter, D. C. Allan, T. A. Arias, and J. D. Joannopoulos, *Rev. Mod. Phys.* **64**, 1045 (1992).
 - [31] G. Kresse and J. Furthmüller, *Phys. Rev. B* **54**, 11169 (1996).
 - [32] D. M. Ceperley and B. J. Alder, *Phys. Rev. Lett.* **45**, 566 (1980).
 - [33] Y. Zhang, J. Sun, J. P. Perdew, and X. Wu, *Phys. Rev. B* **96**, 035143 (2017).
 - [34] R. Resta, *Rev. Mod. Phys.* **66**, 899 (1994).
 - [35] R. Resta and D. Vanderbilt, *Physics of Ferroelectrics* pp. 31–68 (2007).
 - [36] N. A. Spaldin, *Journal of Solid State Chemistry* **195**, 2 (2012).
 - [37] R. A. Evarestov and A. V. Bandura, *Journal of Computational Chemistry* **33**, 1123 (2012).
 - [38] D. Lee, H. Xu, V. Dierolf, V. Gopalan, and S. R. Phillpot, *Phys. Rev. B* **82**, 014104 (2010).
 - [39] S. V. Streltsov, A. S. Mylnikova, A. O. Shorikov, Z. V. Pchelkina, D. I. Khomskii, and V. I. Anisimov, *Phys. Rev. B* **71**, 245114 (2005).
 - [40] E. I. Paredes Aulestia, Y. W. Cheung, Y.-W. Fang, J. He, K. Yamaura, K. T. Lai, S. K. Goh, and H. Chen, *Applied Physics Letters* **113**, 012902 (2018).
 - [41] T. Qi, M. T. Curnan, S. Kim, J. W. Bennett, I. Grinberg, and A. M. Rappe, *Phys. Rev. B* **84**, 245206 (2011).
 - [42] C. Lin, C. Mitra, and A. A. Demkov, *Phys. Rev. B* **86**, 161102 (2012).
 - [43] U. Aschauer, R. Pfenninger, S. M. Selbach, T. Grande, and N. A. Spaldin, *Phys. Rev. B* **88**, 054111 (2013).
 - [44] Z. Zhou, D. Chu, and C. Cazorla, *Sci. Rep.* **11**, 11499 (2021).
 - [45] C. Freysoldt, B. Grabowski, T. Hickel, J. Neugebauer, G. Kresse, A. Janotti, and C. G. Van de Walle, *Rev. Mod. Phys.* **86**, 253 (2014).

- [46] A. Janotti, J. B. Varley, M. Choi, and C. G. Van de Walle, *Phys. Rev. B* **90**, 085202 (2014).
- [47] A. Sarkar and G. G. Khan, *Nanoscale* **11**, 3414 (2019).
- [48] F. Gunkel, D. V. Christensen, Y. Z. Chen, and N. Pryds, *Applied Physics Letters* **116**, 120505 (2020).
- [49] S. Y. Ren, J. D. Dow, and D. J. Wolford, *Phys. Rev. B* **25**, 7661 (1982).
- [50] J. Robertson, *Journal of Applied Physics* **93**, 1054 (2003).
- [51] S. Lany and A. Zunger, *Phys. Rev. B* **78**, 235104 (2008).
- [52] A. Svane, N. E. Christensen, L. Petit, Z. Szotek, and W. M. Temmerman, *Phys. Rev. B* **74**, 165204 (2006).
- [53] B. Huang, M. Yoon, B. G. Sumpter, S.-H. Wei, and F. Liu, *Phys. Rev. Lett.* **115**, 126806 (2015).
- [54] T. Xu, T. Shimada, Y. Araki, M. Mori, G. Fujimoto, J. Wang, T.-Y. Zhang, and T. Kitamura, *npj Comput Mater* **5**, 23 (2019).
- [55] N. F. Mott, *Proceedings of the Physical Society. Section A* **62**, 416 (1949).
- [56] J. Kuneš, A. V. Lukoyanov, V. I. Anisimov, R. T. Scalettar, and W. E. Pickett, *Nature Materials* **7**, 198 (2008).
- [57] J. Kuneš, D. M. Korotin, M. A. Korotin, V. I. Anisimov, and P. Werner, *Phys. Rev. Lett.* **102**, 146402 (2009).
- [58] A. O. Shorikov, A. V. Lukoyanov, V. I. Anisimov, and S. Y. Savrasov, *Phys. Rev. B* **92**, 035125 (2015).
- [59] L. Huang, Y. Wang, and P. Werner, *EPL (Europhysics Letters)* **119**, 57007 (2017).
- [60] C. S. Yoo, B. Maddox, J.-H. P. Klepeis, V. Iota, W. Evans, A. McMahan, M. Y. Hu, P. Chow, M. Somayazulu, D. Häusermann, et al., *Phys. Rev. Lett.* **94**, 115502 (2005).
- [61] E. Greenberg, I. Leonov, S. Layek, Z. Konopkova, M. P. Pasternak, L. Dubrovinsky, R. Jeanloz, I. A. Abrikosov, and G. K. Rozenberg, *Phys. Rev. X* **8**, 031059 (2018).
- [62] I. Leonov, A. O. Shorikov, V. I. Anisimov, and I. A. Abrikosov, *Phys. Rev. B* **101**, 245144 (2020).
- [63] Q. Qiao, Y. Zhang, R. Contreras-Guerrero, R. Droopad, S. T. Pantelides, S. J. Pennycook, S. Ogut, and R. F. Klie, *Applied Physics Letters* **107**, 201604 (2015).
- [64] K. Nishida, M. Osada, J. Sakai, N. Ito, T. Katoda, R. Ikariyama, H. Funakubo, H. Moriwake, and T. Yamamoto, *Journal of the Ceramic Society of Japan* **121**, 598 (2013).

- [65] T.-F. Zhang, X.-G. Tang, Q.-X. Liu, S.-G. Lu, Y.-P. Jiang, X.-X. Huang, and Q.-F. Zhou, *AIP Advances* **4**, 107141 (2014).
- [66] M. D. Glinchuk, E. A. Eliseev, G. Li, J. Zeng, S. V. Kalinin, and A. N. Morozovska, *Phys. Rev. B* **98**, 094102 (2018).
- [67] G. Singh, V. S. Tiwari, and P. K. Gupta, *Journal of Applied Physics* **107**, 064103 (2010).
- [68] S. Banerjee, M. Kumar Bhunia, A. Bhaumik, and D. Chakravorty, *Journal of Applied Physics* **111**, 054310 (2012).
- [69] S. Starschich, S. Menzel, and U. Böttger, *Applied Physics Letters* **108**, 032903 (2016).
- [70] J. Strand, M. Kaviani, D. Gao, A.-M. El-Sayed, V. V. Afanas'ev, and A. L. Shluger, *Journal of Physics: Condensed Matter* **30**, 233001 (2018).
- [71] Y. Peng, G. Han, F. Liu, W. Xiao, Y. Liu, N. Zhong, C. Duan, Z. Feng, H. Dong, and Y. Hao, *Nanoscale Research Letters* **15**, 1 (2020).
- [72] D. R. Islamov, T. M. Zalyalov, O. M. Orlov, V. A. Gritsenko, and G. Y. Krasnikov, *Applied Physics Letters* **117**, 162901 (2020).
- [73] W. Peng, J. Mun, Q. Xie, J. Chen, L. Wang, M. Kim, and T. W. Noh, *npj Quantum Materials* **6**, 48 (2021).
- [74] Y. Noguchi, H. Matsuo, Y. Kitanaka, and M. Miyayama, *Scientific Reports* **9**, 4225 (2019).
- [75] H. Yu, F. Chen, X. Li, H. Huang, Q. Zhang, S. Su, K. Wang, E. Mao, B. Mei, G. Mul, et al., *Nature Communications* **12**, 4594 (2021).
- [76] S. Bredikhin, S. Scharner, M. Klingler, V. Kveder, B. Red'kin, and W. Weppner, *Journal of Applied Physics* **88**, 5687 (2000).
- [77] M. Lu, B. N. Makarenko, Y.-Z. Hu, and J. W. Rabalais, *The Journal of Chemical Physics* **118**, 2873 (2003).
- [78] K. G. Karapetyan, A. A. Kteyan, and R. A. Vardanyan, *Solid State Communications* **140**, 474 (2006).
- [79] K. Lengyel, A. Peter, L. Kovács, G. Corradi, L. Pálfalvi, J. Hebling, M. Unferdorben, G. Dravecz, I. Hajdara, Z. Szaller, et al., *Applied Physics Reviews* **2**, 040601 (2015).
- [80] C. Díaz-Moreno, R. Farías-Mancilla, J. Matutes-Aquino, J. Elizalde-Galindo, F. Espinosa-Magaña, J. González-Hernández, and A. Hurtado-Macías, *Journal of Magnetism and Magnetic Materials* **356**, 82 (2014).
- [81] M. Manikandan, K. Saravana Kumar, N. Aparnadevi, N. Praveen Shanker, and

- C. Venkateswaran, *Journal of Magnetism and Magnetic Materials* **391**, 156 (2015).
- [82] C. Díaz-Moreno, R. Farias, A. Hurtado-Macias, J. Elizalde-Galindo, and J. Hernandez-Paz, *Journal of Applied Physics* **111**, 07D907 (2012).
- [83] C. Wang, J. Sun, W. Ni, B. Yue, F. Hong, H. Liu, and Z. Cheng, *Journal of the American Ceramic Society* **102**, 6705 (2019).
- [84] M. Stengel, P. Aguado-Puente, N. A. Spaldin, and J. Junquera, *Phys. Rev. B* **83**, 235112 (2011).
- [85] T. Kim, D. Puggioni, Y. Yuan, L. Xie, H. Zhou, N. Campbell, P. Ryan, Y. Choi, J.-W. Kim, J. Patzner, et al., *Nature* **533**, 68 (2016).